

Ultrastructural characterization of dark microglia during aging in a mouse model of Alzheimer's disease pathology and in human post-mortem brain samples

Marie-Kim St-Pierre

Department of Molecular Medicine, Université Laval, Québec City, QC

Micaël Carrier

Axe neurosciences, Centre de recherche du CHU de Québec-Université Laval, Québec, QC

Fernando González Ibáñez

Department of Molecular Medicine, Université Laval, Québec City, QC

Eva Šimončičová

Division of Medical Sciences, University of Victoria, Victoria, BC

Marie-Josée Wallman

CERVO Brain Research Center, Quebec, QC

Luc Vallières

Axe neurosciences, Centre de recherche du CHU de Québec-Université Laval, Québec, QC

Martin Parent

CERVO Brain Research Center, Quebec, QC

Marie-Eve Tremblay (✉ evetremblay@uvic.ca)

Division of Medical Sciences, University of Victoria, Victoria, BC

Research Article

Keywords: Microglia, dark microglia, ultrastructure, Alzheimer's disease, human post-mortem brain samples, dystrophic neurites, amyloid-beta

Posted Date: June 21st, 2022

DOI: <https://doi.org/10.21203/rs.3.rs-1751270/v1>

License:  This work is licensed under a Creative Commons Attribution 4.0 International License.

[Read Full License](#)

Abstract

A diverse heterogeneity of microglial cells was previously described in Alzheimer's disease (AD) pathology, including dark microglia, a state characterized by ultrastructural markers of cellular stress. To provide novel insights into the roles of dark microglia during aging in the context of AD pathology, we performed a quantitative density and ultrastructural analysis of these cells using high-throughput scanning electron microscopy in the ventral hippocampus CA1 *stratum lacunosum-moleculare* of 20-month-old APP-PS1 vs C57BL/6J male mice. The density of dark microglia was significantly higher in APP-PS1 vs C57BL/6J mice, with these cells accounting for nearly half of all microglia observed near amyloid-beta (A β) plaques. This dark microglial state interacted more with dystrophic neurites compared to other APP-PS1 microglia and possessed glycogen granules, associated with a metabolic shift toward glycolysis, which provides the first ultrastructural evidence of their presence in microglia. Dark microglia were further observed in aging human post-mortem brain samples showing similar ultrastructural features as in mouse. Overall, our results provide a quantitative ultrastructural characterization of a microglial state associated with cellular stress (i.e., dark microglia) that is primarily restricted near A β plaques and dystrophic neurites. The presence of this microglial state in the aging human post-mortem brain is further revealed.

Introduction

Alzheimer's disease (AD) is a neurodegenerative disease associated with aging, which is characterized by the accumulation of intracellular neurofibrillary tangles (NFT) consisting of hyperphosphorylated tau and extracellular amyloid-beta (A β), which can form fibrillar A β plaques (1). These pathological signs are associated with neuronal and synaptic loss, the latter representing one of the best correlates for cognitive decline across several brain regions, including the hippocampus, notably important for learning and memory as well as emotional regulation (1,2). Hippocampal atrophy is a common feature of AD that can be observed in other dementias (e.g., vascular, frontotemporal lobar) and during normal aging (3,4). The hippocampus is composed of several subregions, one of which, the CA1, is the first hippocampal area affected by pathological signs of AD, including the appearance of NFTs and A β plaques (5), as well as sustained (neuro)inflammation (6–9).

Recent genome-wide associated studies (GWAS) have shown that numerous gene variants linked with a higher risk of developing late-onset AD (LOAD) [i.e., triggering receptor expressed on myeloid cells 2 (*trem2*), bridging integrator 1 (*bin1*), myeloid cell surface antigen CD33 (*cd33*), apolipoprotein E (*apoe*)] affect the function of microglia (10–12), the resident immune cells of the central nervous system (CNS). Microglia have been shown to participate in the development of tau pathology (13), notably through synaptic spreading (14) and early on during disease progression in the compaction, formation and elimination of A β plaques across mouse models of AD pathology (15–17). This evidence strongly suggest that this brain immune cell plays a crucial role in driving the pathogenesis of this neurodegenerative disease.

Microglia first originate from the yolk sac to colonize the CNS in mouse starting around embryonic day (E) 9.5 (18) corresponding to the 4–5th week of gestation in humans (19–21), after which they proliferate, migrate to their respective territory, and perform various physiological functions crucial for the development and maintenance of CNS homeostasis (22–26). These cells possess highly dynamic processes that survey the parenchyma for insults and cues, both of endo- and exogenous natures (27,28). Beside their surveying functions, microglia are key players in synaptic plasticity, where they can release brain-derived neurotrophic factor promoting synapse formation (29), nibble (trogocytosis) (30) or phagocytose partially or entirely weaker synapses, and dissociate pre- and post-synaptic elements to modify synaptic connectivity (synaptic stripping) (31–33).

In pathological conditions, such as AD, microglial features and functions are altered, a change observed during the onset and progression of the disease. Various microglial states, a term defining microglial groups with distinct characteristics (34), were investigated in mouse models of AD pathology, including dystrophic microglia (also termed senescent microglia in the literature) which are positive for L-ferritin, possess lipofuscin deposits and distinct morphological features (i.e., spherical swellings in their tortuous processes) (35–39). In addition, both in human samples (40–42) and mouse models of AD pathology (43), microglia agglomerate near A β plaques and accumulated dystrophic neurites, while in mouse models AD pathology, they were shown to restrict plaque growth and reduce the overall amyloid load via their phagocytosis of extracellular A β (16,17,44–48). However, later in the disease process, microglia become unable to perform their critical phagocytic functions properly, thereby resulting in increased pathology (12,49–53).

While still under debate, plaque-associated microglia were shown to shift their metabolism to anaerobic glycolysis rather than oxidative phosphorylation, allowing these cells to quickly but less efficiently, generate the adenosine triphosphate (ATP) required for their functions (54–56). This results in an increased production of reactive oxygen species (ROS) (57), which can structurally and functionally alter cellular organelles such as mitochondria and/or the endoplasmic reticulum (ER) (58–60). In addition, previous work in 5xFAD mice, a mouse model of AD pathology, and following A β exposure in cultured primary microglia from neonatal mice, identified that this metabolic switch in microglia was accompanied by a pro-inflammatory signature (54). Minhas *et al.* further revealed that inhibiting this metabolic shift, associated with pro-inflammatory responses in the periphery and CNS, could reverse age-related cognitive decline in mice (61).

Beyond this metabolic alteration, a wide array of microglial states were recently uncovered in mouse models of AD pathology. The A β plaque-associated microglial signature was characterized by an increased expression of genes associated with LOAD (e.g., *inpp5d*, *trem2*, *apoe*, *tyrobp*) (11,12). These microglia, located near A β plaques, further exhibited a unique signature [e.g., disease-associated microglia (DAM) (62), neurodegenerative phenotype (MgND) (63), activated-response microglia (ARM) (11)], as well as diverse ultrastructural alterations (64,65) that corroborate the incredibly diverse nature of microglia described in AD pathology (43,66). The various microglial states observed in mouse models of AD pathology, which recreate either and/or the A β deposition and NFTs (67), also exhibit a similarly

reduced expression of homeostatic genes (e.g., *tmem119*, *p2ry12*, *cx3cr1*). In line with these findings, previous studies from our group identified a microglial state, the dark microglia, which are found nearby fibrillar A β in middle-age, 14-month-old APP-PS1 mice [mouse model of AD with a Swedish mutation in the APP and a humanized presenilin (PSEN1)] (64,65).

Dark microglia, which are immunonegative for the homeostatic microglial marker P2RY12 and weakly positive for CX3CR1 and Iba1, were identified based on their ultrastructural markers of cellular stress (e.g., condensed cyto- and nucleoplasm, dilated ER, altered mitochondria) distinguishing them from other microglia (referred hereafter as typical microglia). Dark microglia were found to interact extensively with blood vessels, synaptic elements (axon terminals and dendritic spines showing dystrophy) and display a strong immunoreactivity for cluster of differentiation molecule 11B (CD11b) and TREM2 (64), a receptor which appears crucial for the appearance of several disease-associated microglial states (DAM, MgND) (62,63). A previous study by Bisht *et al.* revealed that dark microglia can reach a density up to 34 cells per mm² in the hippocampus CA1 of middle-age 14 month-old APP-PS1 male mice, compared to 11 cells per mm² in age-matched controls and 3 cell per mm² found in younger 3-month-old controls (64). Their frequent interactions with dystrophic synaptic elements and the vasculature have suggested key roles in their remodeling, which are particularly exacerbated in AD pathology, hence resulting in synaptic loss and blood-brain barrier disruption (68,69).

While dark microglia were previously observed near A β plaques and dystrophic neurites among the ventral hippocampus CA1 of APP-PS1 mice (64,65), their relationship to AD hallmarks (A β plaques, dystrophic neurites), other elements of the CNS parenchyma, and their ultrastructural markers [i.e., dilated ER, altered mitochondria] remained to be quantitatively analyzed. As aging is the main risk factor for developing LOAD (3), we studied microglial heterogeneity in 20-month-old male mice, a timepoint corresponding to an age range between 56 and 69 years in human individuals, a timeframe where most cases are diagnosed (3,70). In this study, we aimed to quantify the density, distribution and features of dark vs typical microglia based on their distance to A β plaques and dystrophic neurites in 20-month-old APP-PS1 male mice compared to age-matched C57BL/6J male mice. Our observations were conducted in the ventral hippocampus CA1 *stratum lacunosum-moleculare*, where we previously identified dark microglia (Bisht *et al.*, 2016), using high-resolution scanning electron microscopy (SEM). Dark microglia were almost exclusively localized nearby A β plaques and dystrophic neurites in aged APP-PS1 mice contrary to age-matched C57BL/6J controls. Moreover, we found that the dark microglia interacted more frequently with dystrophic vs non-dystrophic axon terminals. While dark microglia often displayed altered mitochondria and dilated ER/Golgi apparatus, both the cells' distribution and mouse genotype accounted for their prevalence of these ultrastructural markers of cellular stress. Glycogen granules, previously not identified in microglia (71,72), were further observed in the cytoplasm of both typical and dark microglia located nearby A β plaques and dystrophic neurites, with a higher prevalence encountered in dark microglia. Finally, we confirmed for the first time the presence of dark microglia displaying similar features as their mouse counterparts in the parahippocampal gyrus and hippocampal head of middle-aged and aged human post-mortem brain samples.

Methods

Animals and mouse brain tissue cutting

All experiments were performed according to the guidelines of the Institutional Animal Ethics Committees, the Canadian Council on Animal Care, as well as the Animal Care Committee of Université Laval. Four, 8 and 20-month-old C57BL/6J and APP^{Swe}-PS1 Δ e9 male mice (No. 34832-JAX, Jackson Laboratory, Maine, USA) ($n = 4$) on a C57BL/6J background (73) were housed under a 12 h light-dark cycle at 22–25°C with *ad libitum* access to food and water. While AD affects both males and females [with females being at higher risk notably due to their increased longevity (74)], we performed the experiments on males as this sex was previously used to investigate the presence of dark microglia in 14-month-old APP-PS1 and C57BL/6J mice (64). The experimental mice were injected with 10 g/kg Methoxy-X04 (Tocris Bioscience, cat# 4920, Bristol, United Kingdom), allowing for the screening of fibrillar A β with fluorescence microscopy (75). For electron microscopy experiments, mice were anesthetized 24 h later by i.p. injection of sodium pentobarbital (80 mg/kg), followed by transcardial perfusion using 3.5% acrolein (diluted in phosphate buffer (PB): 100 mM at pH 7.4) and 4% paraformaldehyde [PFA, diluted in phosphate-buffered saline (PBS): 50 mM at pH 7.4]. Fifty-micrometer thick coronal brain sections were then generated in ice-cold PBS using a vibratome (Leica VT1000S) and kept at -20°C in cryoprotectant solution [20% (v/v) glycerol and 20% (v/v) ethylene glycol in PBS] until further experimentation (76).

Human brain tissue cutting and immunostaining

Coronal hippocampal sections containing the entorhinal cortex, hippocampal head, CA1, CA2 and parahippocampal gyrus from middle-aged and aged individuals (male, 45 years old; female, 81 years old; both 18 h post-mortem interval) were obtained from the brain bank located at the CERVO Brain Research Center (QC, Canada). The brain bank and handling of the post-mortem human tissues were approved by the Ethics Committee of the Institut Universitaire en Santé Mentale de Québec and Université Laval. Written consent was obtained for the use of post-mortem tissues and all analyses were performed in line with the Code of Ethics of the World Medical Association. Brains were sectioned along the midline and hemibrains were cut coronally into 2-cm thick samples. The latter were incubated 3 days at 4°C in 4% PFA and stored at 4°C in PBS with 15% sucrose and 0.1% sodium azide. Regions of interest were subsequently cut into 50 μ m-thick sections using a vibratome and stored at -20°C in cryoprotectant solution until immunostaining (65).

For immunostaining, human brain sections containing the regions of interest (CA1, CA2, parahippocampal gyrus, enthorinal cortex, hippocampal head) were first washed in PBS and quenched for 5 min in 0.3% H₂O₂ diluted in PBS. Following the quenching step, sections were washed 3 times 10 min in PBS and incubated for 30 min in 0.1% NaBH₄ diluted in PBS. After washing 3 times 10 min in PBS, the sections were blocked in a solution containing 10% fetal bovine serum, 3% bovine serum albumin and 0.01% Triton X-100 [in Tris-buffered saline (TBS), 50 mM, pH 7.4] for 1 h. The sections were then incubated overnight at 4°C in primary rabbit antibody against ionized calcium binding adaptor molecule 1

(Iba1, FUJIFILM Wako Chemical Virginia, USA, cat# 019-19741) diluted 1/1000 in the blocking buffer. The following day, the sections were washed 3 times 10 min in TBS and incubated in biotinylated goat anti-rabbit secondary antibody (1/300 in TBS, Jackson ImmunoResearch, Philadelphia, USA, cat# 111-066-046). After 3 times 10 min washes in TBS, the sections were incubated for 1 h in an avidin-biotin solution (1/100 in TBS; VECTASTAIN®, Vector Labs, California, USA, cat# VECTPK6100) and washed 3 times 10 min in TBS. The staining was then revealed in a solution containing 0.05% 3-3'-diaminobenzidine (DAB, Millipore Sigma, Massachusetts, USA, D5905-50TAB) and 0.015% H₂O₂ in 100 mM Tris-HCl.

Mouse and human sample preparation for electron microscopy and imaging

Brain sections containing the ventral hippocampus (Bregma -2.92 to 3.64 mm) from 4, 8 and 20-month-old APP-PS1 and age-matched C57BL/6J mice (n = 3–4), as well as immunostained post-mortem human samples containing the regions of interest (CA1, CA2, parahippocampal gyrus, entorhinal cortex, hippocampal head) were processed for SEM. The protocol for the sample preparation was recently detailed in St-Pierre *et al.*, (77). Briefly, the sections were washed in PB and incubated 1 h in a solution containing equal volume of 4% osmium tetroxide (EMS, Pennsylvania, USA, cat# 19190) and 3% potassium ferrocyanide (Sigma-Aldrich, Ontario, Canada, cat# P9387) in PB. After washing in PB, the sections were incubated 20 min in a filtered 1% thiocarbohydrazide solution (diluted in MilliQ water; Sigma-Aldrich, Ontario, Canada, cat# 223220) followed by a second 30 min incubation with 2% aqueous osmium tetroxide (diluted in MilliQ water). Once the sections were post-fixed, they were dehydrated in ascending concentrations of ethanol for 10 min each (2 x 35%, 50%, 70%, 80%, 90%, 3 x 100%) and washed 3 times for 10 min with propylene oxide (Sigma-Aldrich, #cat 110205-18L-C). The tissues were then embedded in Durcupan resin (20 g component A, 20 g component B, 0.6 g component C, 0.4 g component D; Sigma Canada, Toronto, cat# 44610) for 24 h. The following day, for flat-embedding, the resin-infiltrated brain sections were placed onto fluoropolymer films (ACLAR®, Pennsylvania, USA, Electron Microscopy Sciences, cat# 50425-25) painted with resin and kept at 55°C in a convection oven for 3 days to allow for resin polymerization.

After resin polymerization, areas containing the regions of interest from the mouse and human samples were excised and glued onto resin blocks for ultramicrotomy sectioning. Using a Leica ARTOS 3D ultramicrotome, 70-nm thick sections from these areas were cut (2–6 levels, ~5–6 µm apart) and collected on silicon wafers for imaging by SEM or on copper mesh grids for transmission electron microscopy imaging. With SEM, pictures were acquired at a resolution of 25 nm for the density analysis and 5 nm of resolution for the ultrastructural analysis of microglia using a Zeiss Crossbeam 540 SEM, operating at a 1.4 kV voltage and 1.2 nA current. The software Zeiss Atlas 5 (Fibics, Ottawa) was used to stitch and export the images in .tif format. Sections from 4-month-old APP-PS1 and C57BL/6J male mice were additionally screened for dark microglia's presence using a JOEL JEM-1400 transmission electron microscope operated at 80 kV and microglia were imaged with a Gatan SC-1000 digital camera at 6000X magnification.

Quantitative analysis of typical vs dark microglia in APP-PS1 and C57BL/6J mice

For the density analysis in mouse samples, images from 4 animals per group captured in the CA1 *stratum lacunosum-moleculare* were blinded to the experimental condition to avoid introducing bias. In each animal, 2–6 levels (~5–6 μm apart) were analyzed to determine the average density of different microglial states. Typical and dark microglia, identified by their ultrastructural features detailed below, were further categorized based on their distance to fibrillar A β plaques and dystrophic neurites. Microglia were determined to be near an A β plaque if the most proximal point of their cell body was less than 25 μm away from the plaque core. The density of typical and dark microglia, as well as the ratio of dark microglia over all microglia imaged, based on their distance from AD hallmarks, was calculated in 25 nm resolution pictures. Dark microglia were differentiated from typical microglia by their electron-dense cyto- and nucleoplasm and a distinctive loss of the nuclear heterochromatin pattern (64,65,76,78). Intermediate microglia were identified by the presence of a less-defined heterochromatin pattern and dark cytoplasm similar to the dark microglia, and their markers of cellular stress, such as ER dilation and altered mitochondria (65,77). Intermediate and dark microglia were pooled for the density and ultrastructural analyses of dark microglia as both cell states present a condensation of their nucleo- and cytoplasm as well as ultrastructural markers of cellular stress (65).

For the ultrastructural analysis, 9–12 microglia per animal per localization to plaques (far or near), state (typical or dark) and genotype (C57BL/6J vs APP-PS1) were imaged at 5 nm of resolution within the CA1 *stratum lacunosum-moleculare*, where dark microglia were previously found (64,65). The images were blinded to the experimental condition to prevent bias. To quantify ultrastructural changes, we analyzed 111 microglial cell bodies in total (27–29 microglia per condition), a sample size which was considered sufficient to obtain statistical power based on the G*Power software V3.1 (effect size of 0.4 and power of 0.95 estimated to 112 individual cells). A similar effect size was previously used to quantitatively assess microglial ultrastructure (79). To compare dark vs typical microglia's interactions with AD hallmarks (dystrophic neurites, A β plaques), we analyzed 55 microglial cell bodies (27–28 microglia per condition) in the *stratum lacunosum-moleculare*, which was considered sufficient to obtain a large effect size of 0.9 using G*Power software V3.1 (power of 0.9) (80). No immunostaining was performed to allow the experimenter to observe the electron density of the cytoplasm/nucleoplasm and examine the presence or absence of glycogen granules. The identification of microglia and their cytoplasmic content was previously described in detail (81). Typical microglia were identified by their heterochromatin pattern and differentiated from oligodendrocytes by their long and narrow ER stretches, and presence of diverse inclusions (e.g., lysosomes, lipofuscin granules) dispersed heterogeneously in their cytoplasm (81). In addition to the ultrastructural characteristics examined at 25 nm of resolution, the presence of oxidative stress markers (e.g., altered mitochondria, dilated ER), and dystrophic neurites were further used to identify dark and intermediate microglia at 5 nm of resolution (64,76).

Lysosomes were identified by their circular and homogenous (primary) or heterogenous (secondary, tertiary) content. Secondary lysosomes were larger than primary lysosomes and often contained empty phagosomes. Tertiary lysosomes were the largest and possessed large lipid bodies in addition to phagosomes (65,82). Lipid bodies, either contained in a lysosome or within the cytoplasm, were characterized by their electron-dense circular outline with a homogenous and electron-dense interior.

Lipofuscin granules were identified by their electron-dense content with a unique fingerprint-like pattern. Fully digested (electron-lucent) or partially digested (electron-lucent with cellular content) phagosomes were identified by their defined circular shape and electron-lucent interior. Autophagosomes presented as double-membrane endosomes with a circular shape and an interior with a similar appearance to the cell's cytoplasm (76,77,81,83).

Fibrillar contents, which were previously described in (64,65), are characterized by their elongated shape and fibrils, with electron-dense patches (84,85). Dystrophic neurites (axon terminals, dendrites and dendritic spines) contacted by the microglial cell bodies were characterized by an accumulation of electron-dense autophagic vacuoles and mitochondria, together with a swollen appearance. Fibrillar A β plaques associated with microglial cell bodies were identified by their heterogenous fibrils forming a tree-like shape (75,77). Myelinated axons were identified by their electron-dense sheaths and granular cytoplasm often containing mitochondria (86). Extracellular digestion and extracellular space consisted of electron-lucent space devoid of a membrane delineation located next to a microglia and containing (digestion) or not (space) partially-digested cellular elements (87). Axon terminals were defined by their numerous synaptic vesicles, while dendritic spines were recognized by their postsynaptic density (83,88). Microglial contacts with synaptic elements were categorized as axon terminals, dendritic spines or both (when the two elements and synaptic cleft were contacted simultaneously) (77). Microglia were considered to be associated with the vasculature if the distance between their cell body plasma membrane and the vascular basement membrane was under 150 nm [justavascular microglial cell soma were previously considered to be associated with the vasculature when closer to 10 μ m using *in vivo* 2-photon microscopy (89)].

Endoplasmic reticulum cisternae were characterized by their long and narrow stretches found in the microglial cytoplasm (81). Dilated ER and Golgi apparatus were identified by the swollen electron-lucent appearance of these organelles (determined as dilated if the cisternae diameter was over 100 nm) (77). Mitochondria were identified by their electron-dense appearance, double membrane, numerous cristae, and circular shape. Altered mitochondria were characterized by a deterioration of the outer membrane, degradation of the cristae (electron-lucent pockets) or "holly" shape (i.e., mitochondria forming a donut shape) (76). Mitochondria were defined as elongated if their length was over 1000 nm (90). Glycogen granules were identified by their electron-dense, small and rounded shape with a diameter of 22–40 nm. This is in line with the reported literature which identified β -granules in the brain (glycogen granules comprise several g-granules which are termed β -granules) at a maximum size of 42 nm, while the average size is approximately 20–30 nm (91). Microglia containing more than 5 of these granules were determined to be positive to prevent a false-positive identification.

To assess microglial area, perimeter and morphology, the outline of each microglial cell body was traced using the freehand tool in Image J and the shape descriptors i.e., aspect ratio, area, perimeter, solidity, and circularity were assessed. Aspect ratio (AR) refers to the ratio of the height over the width of the microglial cell body. Solidity is calculated by dividing the area of the cell over the convex area and is an indicator of irregular shapes. The closer the value of the solidity is to 1, the less irregular shape the microglial cell

body possesses (86,92). Circularity is calculated as 4π times the area over the perimeter squared. Circularity is an indicator of the cell's shape, where a value closer to 1 indicates a rounder shape and a value near 0 reflects a more elongated shape (65,86,93).

Qualitative analysis of typical vs dark microglia in the human brain samples

Similar to microglia in mouse brains, typical microglial cell bodies in human post-mortem brain samples were identified based on their heterochromatin pattern, presence of lipofuscin deposits and a positive immunoreactivity to Iba1. Dark microglia were further identified based on their electron-dense cyto- and nucleoplasm, while they possessed in these samples an heterochromatin pattern similar to typical microglia. Their cellular content (e.g., phagosomes, mitochondria, lysosomes, lipofuscin granules, ER, Golgi apparatus) and interactions with the CNS parenchyma (axon terminals, dendritic spines, myelinated axons, blood vasculature) were assessed and found to be similar to those in mouse microglia.

Statistical analysis

Prism 9 (v.9.2.0, GraphPad software) was used for statistical analysis in mice. All density and ultrastructure data obtained were tested for their normality using the Shapiro-Wilk test. The quantitative ultrastructural and density comparison of typical microglia in C57BL/6J mice, typical microglia far from plaques in APP-PS1 mice, as well as typical and dark microglia near plaques of APP-PS1 mice was performed with a Kruskal-Wallis One-Way ANOVA followed by a Dunn's *post-hoc* test. The interactions of typical and dark microglia with AD pathology hallmarks was compared with a Mann-Whitney non-parametric t-test. Data are expressed as mean \pm standard error of the mean (SEM). The sample size (n) refers to individual animals for density analysis and individual microglia for ultrastructural analyses as previously performed in ultrastructural studies of microglia (65,82,86,89,90,94,95). Statistically significant differences are reported as * $p < 0.05$, ** $p < 0.01$, *** $p < 0.001$ and, **** $p < 0.0001$.

Results

Dark microglia are highly prevalent in aged APP-PS1 mice compared to age-matched C57BL/6J mice

Dark microglia were previously observed in the ventral CA1 *stratum lacunosum-moleculare* of middle-age 14-month-old APP-PS1 mice, where they were localized nearby A β plaques and dystrophic neurites (64,65,78). These cells were ultrastructurally defined by their condensed electron-dense cyto- and nucleoplasm, accompanied by several markers of oxidative stress (e.g., ultrastructurally altered mitochondria, dilated ER cisternae) (64,76). To investigate and characterize dark microglia during aging, the main risk factor for AD (96), we first determined their distribution using high magnification SEM chip mapping, within the ventral CA1 *stratum lacunosum-moleculare*, which exhibits considerable atrophy in APP-PS1 mice and patients with AD (4,97), and where dark microglia were previously shown to be abundant in 14-month-old C57BL/6J and APP-PS1 mice (64). In particular, the density of dark vs typical microglia was determined among areas associated with A β plaques and dystrophic neurites. Typical microglia were previously shown to exhibit ultrastructural diversity based on their proximity to dystrophic

neurites (65). Previous studies have also shown the association of various microglial states (dark microglia, DAM, MGnD) with A β plaques and dystrophic neurites (62–64).

In the *stratum lacunosum-moleculare*, the density of typical microglia near A β plaques and dystrophic neurites (NTM) was significantly reduced compared to control C57BL/6J typical microglia (CTM) (NTM $18.91 \pm 6.555 \text{ mm}^2$ vs CTM $59.13 \pm 9.170 \text{ mm}^2$, $p = 0.0427$), while no difference was observed for typical microglia located far from A β plaques and dystrophic neurites (FTM) (**Figure 1A**). Conversely, the density of dark microglia was significantly greater near A β plaques and dystrophic neurites (NDM) than far from A β plaques and dystrophic neurites (FDM) (NDM $13.24 \pm 3.827 \text{ mm}^2$ vs FDM $0.7747 \pm 0.7747 \text{ mm}^2$, $p = 0.0417$). A similar trend was observed for dark microglia in age-matched C57BL/6J mice (CDM) (NDM $13.24 \pm 3.827 \text{ mm}^2$ vs CDM $0.8559 \pm 0.8559 \text{ mm}^2$, $p = 0.0733$) (**Figure 1B**). When comparing the density of typical and dark microglia in the APP-PS1 mice based on their distribution near A β plaques and dystrophic neurites, we observed significantly more typical compared to dark microglia farther from A β plaques and dystrophic neurites (FTM $45.04 \pm 8.654 \text{ mm}^2$ vs FDM $0.7747 \pm 0.7747 \text{ mm}^2$, $p = 0.0045$), while no difference was observed for dark and typical microglia near these two AD pathology hallmarks (**Figure 1C**). Dark microglia represented nearly 43% of all microglia found near A β plaques and dystrophic neurites (**Figure 1D**), while their percentage were reduced to 1.4% and 1.2%, respectively, for dark microglia located far from A β plaques and dystrophic neurites and those observed in age-matched C57BL/6J mice.

Dark microglia interact more with dystrophic neurites compared to their typical counterpart in aged APP-PS1 mice

Our results indicate that dark microglia preferentially associate with hallmarks of neurodegeneration in the ventral CA1 *stratum lacunosum-moleculare* of 20-month-old APP-PS1 mice. This specific localization is corroborated by our previous studies where dark microglia were often localized near A β plaques in the ventral CA1 *strata lacunosum-moleculare* and *radiatum* of 14-month-old APP-PS1 mice (64,65). In the current study, we found in the ultrathin sections imaged by SEM that 52.5% of A β plaques were associated with at least one dark microglia within a perimeter of 25 μm . It is likely that the proportion of dark microglia juxtaposing plaques could be higher but was underestimated due to the thinness of the samples (70 nm). To provide further insights into the interactions between A β plaques, dystrophic neurites and dark microglia, we examined two earlier timepoints, i.e., 4 months of age when plaques have started to develop and are yet few in numbers (98,99) and 8 months of age when plaques are starting to appear in this model. In these mice, we confirmed the presence of A β plaques by systemically injecting Methoxy-X04, a fluorescent derivative of congo red that stains A β (75), 24 h prior to the euthanasia, as well as their distinct ultrastructure in SEM (77). We did not identify dark microglia in the 4-month-old APP-PS1 mice devoid of A β plaques and dystrophic neurites, confirming that a significant presence of pathological signs related to A β deposition is crucial for the appearance and accumulation of these cells. By contrast, in the 8-month-old APP-PS1 mice, we observed a similar pattern as in 20-month-old mice, where dark microglia were localized near A β plaques and dystrophic neurites (**Supplementary Figure 1**).

Having shown the necessity of A β plaques and dystrophic neurites for the appearance of dark microglia in the APP-PS1 mice, we decided to further explore the direct interaction of dark vs typical microglia with A β plaques and dystrophic neurites. Dark microglia interacted more with dystrophic neurites than typical microglia (NDM 2.036 ± 0.2931 contact per microglia vs NTM 1.407 ± 0.4929 contact per microglia, $p = 0.0045$) (**Figure 2 C**). More dark microglia compared to typical microglia also directly interacted with at least one dystrophic neurite (NDM $82.14 \pm 7.371\%$ vs NTM $55.56 \pm 9.745\%$, $p = 0.0080$) (**Figure 2 C,E**). Dark microglia and typical microglia made similar numbers of direct contacts with A β plaques (**Figure 2 D,F**). However, both typical and dark microglia directly touching an A β plaque contained fibrillar A β in their cytoplasm, suggesting that the two microglial states actively cooperate in contributing to reducing the A β load.

Dark microglia interact less with parenchymal elements and the vasculature than typical microglia in aged APP-PS1 mice

Dark microglia contacted significantly more dystrophic neurites than typical microglia in 20-month old APP-PS1 mice. To provide insights into the relationship between dark microglia and the CNS parenchyma, we next investigated their direct interactions with apparently healthy, or not exhibiting ultrastructural signs of dystrophy, synaptic elements (axon terminals, dendritic spines), myelinated axons and the vasculature of APP-PS1 mice.

In terms of synaptic relationships, dark microglia located near A β plaques and dystrophic neurites contacted significantly less non-dystrophic elements (axon terminals, dendritic spines, both elements of the same excitatory synapse) than typical microglia located far from A β plaques and dystrophic neurites (NDM 5.429 ± 0.4945 contact per microglia vs FTM 8.448 ± 0.6250 contact per microglia, $p = 0.0064$). Specifically, this change was associated with reduced interactions with axon terminals for dark microglia located near A β plaques and dystrophic neurites compared to typical microglia located far from A β plaques and dystrophic neurites (NDM 4.107 ± 0.4581 contact per microglia vs FTM 6.207 ± 0.5490 contact per microglia, $p = 0.0303$) (**Figure 3F-G**). However, this difference was not observed between dark microglia near A β plaques and dystrophic neurites, typical microglia away from AD pathology hallmarks, and typical microglia in C57BL/6J mice (**Tables 1-2**). This change could be due to dark microglia preferentially interacting more with dystrophic neurites vs non-dystrophic synaptic elements, highlighting a key difference in functional interventions based on the microglial state.

In terms of interactions with axonal myelination, which was found to be affected in AD (100), we found that dark microglia located near A β plaques and dystrophic neurites contacted less myelinated axons compared to typical microglia far from A β plaques and dystrophic neurites and typical microglia in control C57BL/6J mice (NDM 0.0 ± 0.0 contact per microglia vs FTM 0.6207 ± 0.1818 contact per microglia, $p = 0.0035$; NDM 0.0 ± 0.0 contact per microglia vs CTM 0.5556 ± 0.1716 contact per microglia, $p = 0.0152$). Similarly, dark microglia located near A β plaques and dystrophic neurites juxtaposing at least one myelinated axon were significantly reduced in number compared to typical microglia far from the two AD hallmarks and to C57BL/6J typical microglia (NDM $0.0 \pm 0.0\%$ vs CTM $33.33 \pm 9.245\%$, $p =$

0.0144; NDM $0.0 \pm 0.0\%$ vs FTM $37.93 \pm 9.170\%$, $p = 0.0026$) (**Figure 3 H-I**). However, these interactions were similar between dark and typical microglia located near A β plaques and dystrophic neurites, suggesting that this difference in contact with myelinated axons is not due to the proximity to AD pathology hallmarks. Moreover, we confirmed that these changes in parenchymal interactions were not associated with a change in the size of these cells (i.e., increased perimeter or area of the cell body's nucleoplasm and cytoplasm). Indeed, we did not observe any differences in the area, perimeter, and aspect ratio of the dark microglia located near A β plaques and dystrophic neurites compared to all the typical microglia groups (**Figure 4 E-F**). Nevertheless, we found a significant reduction in the circularity (NDM 0.4417 ± 0.03181 a.u. vs NTM 0.5820 ± 0.03226 a.u., $p = 0.0082$; NDM 0.4417 ± 0.03181 a.u. vs FTM 0.5993 ± 0.02212 a.u., $p = 0.0043$) and solidity (NDM 0.8038 ± 0.02264 a.u. vs NTM 0.8620 ± 0.02245 a.u., $p = 0.0324$; NDM 0.8038 ± 0.02264 a.u. vs FTM 0.8891 ± 0.01269 a.u., $p = 0.0164$) of the dark microglia observed near A β plaques and dystrophic neurites compared to typical microglia both localized near and far from A β plaques and dystrophic neurites in APP-PS1 mice. This finding suggests an increased irregularity of their cell body shape (**Figure 4**), previously associated with membrane ruffling (101) and the presence of minute pseudopodia (102).

While our previous studies identified dark microglia near the vasculature (e.g., mouse models of chronic stress, CX3CR1 knockout, middle-aged C57BL/6J and APP/PS1 mice), we rarely observed this association in the aged APP-PS1 mice. This change may be attributed to the genotype rather than the cellular state, as all microglia (both typical and dark) observed in the APP-PS1 mice interacted significantly less with the vasculature compared to C57BL/6J typical microglia, regardless of their distance to A β plaques and dystrophic neurites (NDM $3.571 \pm 3.571\%$ vs CTM $33.33 \pm 9.245\%$, $p = 0.0038$; NTM $3.704 \pm 3.704\%$ vs CTM $33.33 \pm 9.245\%$, $p = 0.0045$; FTM $6.897 \pm 4.789\%$ vs CTM $33.33 \pm 9.245\%$, $p = 0.0133$) (**Figure 3 G**). This drastic difference in dark microglial vascular interactions observed in the aged APP-PS1 mice compared to the controls could be associated with a previously observed reduced volume of cerebral vasculature near A β plaques, a phenomenon suggested to be caused by non-productive angiogenesis resulting in vascular scars near A β plaques (103).

Overall, in parallel with an increased interaction with dystrophic neurites, dark microglia also interacted less with non-dystrophic axon terminals and myelinated axons, as well as blood vessels, highlighting their preferential interactions with dystrophic neurites during aging and A β pathology.

Dark microglia possess more ultrastructural markers of cellular stress compared to typical microglia in aged C57BL6/J mice

Considering that dark microglia were previously described as phagocytic cells with several ultrastructural markers of cellular stress (e.g., altered mitochondria, dilated ER, electron-dense cyto- and nucleoplasm) (64,65,76), we next investigated the cellular content of these cells in the context of aging and A β pathology. Although we noticed a main effect due to the genotype (C57BL/6J vs APP-PS1) ($p = 0.0331$) at 20 months of age, we did not find significant differences in the number of phagosomes (partially and fully digested) and number of cells containing at least one phagosome between all the microglial groups

examined (C57BL/6J typical microglia, APP-PS1 typical microglia far vs near A β plaques and dystrophic neurites, APP-PS1 dark microglia near A β plaques and dystrophic neurites). All the APP-PS1 microglia, both typical and dark, showed a significant increase in their number of altered mitochondria compared to C57BL/6J typical microglia (NDM 3.464 ± 0.6289 per microglia vs CTM 0.3704 ± 0.1087 per microglia, $p < 0.0001$; NTM 1.889 ± 0.4347 per microglia vs CTM 0.3704 ± 0.1087 per microglia, $p = 0.0072$; FTM 1.207 ± 0.1815 per microglia vs CTM 0.3704 ± 0.1087 per microglia, $p = 0.0362$). Additionally, more APP-PS1 dark and typical microglia contained ultrastructurally-altered mitochondria compared to C57BL/6J typical microglia (NDM $78.57 \pm 7.897\%$ vs CTM $33.33 \pm 9.245\%$, $p=0.0030$; NTM $70.37 \pm 8.955\%$ vs CTM $33.33 \pm 9.245\%$, $p = 0.0287$; FTM $72.41 \pm 8.447\%$ vs CTM $33.33 \pm 9.245\%$, $p = 0.0147$) (**Figure 5 F,I**).

In addition, dark and typical microglia near A β plaques and dystrophic neurites showed a significant increase in the number of dilated ER compared to the C57BL/6J typical microglia (NDM 2.071 ± 0.4740 per microglia vs CTM 0.2222 ± 0.1111 per microglia, $p = 0.0010$; NTM 1.593 ± 0.3968 per microglia vs CTM $.2222 \pm 0.1111$ per microglia, $p = 0.0081$). Similarly, we found an increased number of microglia near A β plaques and dystrophic neurites containing at least one dilated ER cisternae compared to C57BL/6J typical microglia (NDM $60.71 \pm 9.399\%$ vs CTM $14.81 \pm 6.967\%$, $p = 0.0036$; NTM $55.56 \pm 9.745\%$ vs CTM $14.81 \pm 6.967\%$, $p = 0.0154$). Since both dark and typical microglia near A β plaques and dystrophic neurites contained more dilated ER cisternae, the distribution of these cells (i.e., association with A β plaques and dystrophic neurites) was likely underlying this increased prevalence. While dark microglia near A β plaques and dystrophic neurites possess numerous markers of cellular stress, there were no quantitative differences between typical microglia located near vs far from A β plaques and dystrophic neurites (**Figure 2**). In short, both dark and typical microglia in APP-PS1 mice can possess signs of cellular stress, denoting the impact of AD pathology on the two microglial states.

Dark and typical microglia located near A β plaques and dystrophic neurites contain glycogen granules in aged APP-PS1 mice

While normally absent in microglia or observed at very low levels (72,104), we found ultrastructural evidence of glycogen granules in the cytoplasm of dark and typical microglia located near A β plaques and dystrophic neurites. Sequestered glycogen, along with the predominant metabolic shift to glucose metabolism, was previously associated in myeloid cells with a pro-inflammatory response (61). The percentage of dark microglia containing glycogen granules was significantly higher compared to typical microglia located far from A β plaques and dystrophic neurites and typical microglia in C57BL/6J control mice (NDM $60.71 \pm 9.399\%$ vs CTM $0 \pm 0\%$, $p < 0.0001$; NDM $60.71 \pm 9.399\%$ vs FTM $3.448 \pm 3.488\%$, $p < 0.0001$). These glycogen granules were distributed throughout the microglial cytoplasm of microglial cells located near A β plaques and dystrophic neurites (**Figure 6**). An accumulation of glycogen granules was observed in ~60% of all dark microglia observed in the *stratum lacunosum-moleculare* of APP-PS1 mice, while ~30% of typical microglia near A β plaques and dystrophic neurites contained a minimum of five glycogen granules within their cytoplasm (NDM $60.71 \pm 9.399\%$ vs NTM $29.63 \pm 8.955\%$, $p = 0.0405$). We observed a very low percentage (< 3%) of typical microglia located far from A β plaques and

dystrophic neurites containing cytoplasmic glycogen granules, while the latter were not found in any typical microglia in the C57BL/6J mice (**Figure 6**). These findings indicate that glycogen granule accumulation is largely associated with hallmarks of AD pathology and neurodegeneration. This ultrastructural finding suggests that microglia located near A β plaques and dystrophic neurites possess a feature traditionally associated with glycolysis, which is further exacerbated by the cellular state (dark vs typical microglia).

Dark microglia are found in human post-mortem brain samples from middle-aged and aged individuals

While dark microglia were previously reported at adulthood in several mouse models of pathology [e.g., prenatal and maternal immune activation, middle-aged APP-PS1, chronic stress, CX3CR1 knockout, R6/2 model of Huntington's disease; (64,78,94,105,106)], their presence in the human brain had yet to be reported. We observed dark cells possessing ultrastructural features of dark microglia in the hippocampal head of post-mortem brain samples from a 49-year-old man and in the parahippocampal gyrus from an 81-year-old woman (both with a post-mortem interval of 18 h). Similar to dark microglia described in mice, dark microglia in these human brains were characterized by their electron-dense cyto- and nucleoplasm, however, still possessing in this case a relatively well-defined eu- and heterochromatin pattern. In addition, similar to the dark microglia described in mice, numerous altered mitochondria, identified by the electron-lucent space within the organelle and deterioration of the outer and inner membranes, were observed in the human dark microglia (**Figure 7 A-C**). Several lipofuscin granules, which are considered a marker of cellular senescence (107), were observed in the cytoplasm of the human dark microglia (**Figure 7 A-C**). Moreover, dark microglia were seen making direct contacts with multiple axon terminals. We further did not observe a positive Iba1 immunostaining on the human dark microglia, compared to the low to no immunoreactivity to Iba1 observed in the dark microglia from mice (64), suggesting, along with the still-visible chromatin pattern, that these microglia are an intermediate dark state (**Figure 7 D-F**).

Discussion

Microglial heterogeneity has become a topic of high interest with the discovery of numerous microglial states in mouse models of AD pathology, such as the DAM (62), MGnD (63) and plaque-associated microglia (PAM) (41, 44, 108–110). The features distinguishing these states from typical microglia include an absent or reduced gene expression or immunoreactivity for microglial homeostatic markers (e.g., P2RY12, TMEM119), a unique molecular signature (e.g., *Ipl*, *clec7a*, *cd9*) (34), as well as diverse proposed roles which can be beneficial or detrimental depending on the context (e.g., clearance of A β , propagation of tau) (12, 108). The dark microglia, a state previously identified in adult mouse models of pathology, including AD, was characterized by its distinctive ultrastructural appearance (i.e., electron-dense cyto- and nucleoplasm, altered mitochondria, dilated ER cisternae, loss of heterochromatin pattern). Our previous work has identified the preferential location of these cells near A β plaques and dystrophic neurites, and their extensive interactions with synaptic elements (axon terminals, dendritic

spines, both elements of a same synapse) (64, 65), suggesting a key role in the synaptic dysfunction observed in AD (1).

The current study investigated the distribution and ultrastructure of dark vs typical microglia based on their distance to A β plaques and dystrophic neurites in the ventral hippocampus CA1 *stratum lacunosum-moleculare*, where dark microglia were previously observed in high numbers (64, 65), within 20-month-old APP-PS1 and C57BL/6J male mice. We found that while dark microglia were barely present in aged 20-month-old C57BL/6J male mice, their density increased drastically with A β plaques and dystrophic neurites, reaching 43% of all the microglia found nearby A β plaques and dystrophic neurites in the *stratum lacunosum-moleculare* of age-matched APP-PS1 mice. The exact role of dark microglia in the pathogenesis of AD remains unclear. The importance of dark microglia's interventions near A β plaques and dystrophic neurites is supported by the finding that more than half of all the fibrillar A β plaques observed had at least one dark microglia present within its micro-environment. This presence of dark microglia near A β plaques was likely underestimated as the ultrathin sections examined do not provide a 3D view of the plaques, therefore there were likely many additional cells located above and below the 70 nm plane imaged. Whether dark microglia are a result of their proximity to A β plaques and dystrophic neurites, for instance arising from typical microglia that switch their metabolism to glycolysis which results in cellular stress, remains to be investigated. In addition, the dark microglia preferentially interacted with dystrophic neurites compared to typical microglia observed near A β plaques and dystrophic neurites, a feature that we previously reported without performing yet quantification (64). The internalization of dystrophic neurites was previously attributed to reactive astrocytes in the hippocampus of 6 and 12-month-old APP-PS1 male mice (111). While we did not observe dark microglia internalizing dystrophic elements, a previous study has identified dystrophic neurites inside of dark microglial cells (64). Therefore, it remains inconclusive how dark microglia interact with dystrophic neurites over the course of AD pathology and whether this state results from and/or contributes to the appearance of dystrophic neurites. In addition to our findings in regards to dystrophic neurites and dark microglia, in the current study we showed an increased abundance of ultrastructural markers of cellular stress (altered mitochondria, dilated ER) in the microglia located near A β plaques and dystrophic neurites, together with altered parenchymal interactions (reduced contacts with the vasculature) compared to typical microglia in age-matched C57BL/6J mice. This is in line with our previous findings identifying dilated ER in microglia located near A β plaques and dystrophic neurites in the ventral hippocampus CA1 of 14-month-old APP-PS1 male mice (65).

A distinct feature of plaque-associated microglia is their metabolic shift from a primarily oxidative phosphorylation to glycolysis, known in cancer cells as the Warburg effect (54–57). This shift in plaque-associated microglia was shown to result from the presence of A β (54, 55) and elevated levels of iron (55, 57), an electron-dense metal that can trigger the production of ROS. Iron accumulation in plaque-associated microglia was reported both using mouse models of AD pathology and human post-mortem brain samples (54, 57, 57, 112). The accumulation of iron within microglial states will be interesting to investigate in future studies, as it could account for the electron-dense nature of the dark microglia, the presence of several signs of cellular stress (that can be attributed to oxidative stress, and therefore the

presence of ROS) as well as occurrence of glycogen granules. Glycogen, which is broken down during glycolysis, can be used as an energy source by CNS cells such as astrocytes, and has been shown to be crucial for memory and learning processes (91, 104). Glycogen accumulation in myeloid cells was observed in 20–24-month old C57BL/6J mice, which was attributed to the prostaglandin E₂ (PGE₂)-prostaglandin E₂ receptor 2 (EP2) signaling pathway (61). Inhibition of this pathway in the periphery restored long-term potentiation to youthful levels in the hippocampus CA1, suggesting that this metabolic switch toward glycolysis has detrimental effects on cognitive functions during aging in mice (61). Moreover, microglia observed near A β deposition in 19–20 month-old APP-PS1 male and female mice were found to accumulate iron while expressing 6-phosphofructo-2-kinase/fructose-2,6-biphosphate 3 (PFKFB-3), a regulator of glycolysis (55). In our study, the accumulation of glycogen granules was restricted to microglia (both typical and dark states, but especially dark ones) found nearby A β plaques, suggesting that fibrillar A β could also be a key player in driving this metabolic shift. To the authors' knowledge, this is the first ultrastructural evidence of glycogen granules accumulation in microglia. Glycogen granules were not observed in the human post-mortem brain samples that we examined, probably due to the rapid depletion of glycogen over post-mortem time (104), which prevented their investigation in human dark microglia.

In addition to our quantitative analysis in mice, we report for the first time a prevalence of dark microglia in post-mortem human brain samples, among the parahippocampal gyrus and hippocampal head of from a 45-year-old man and an 81-year-old woman, respectively. Microglia appearing ultrastructurally more electron-dense than typical microglia were previously shown nearby oligodendrocytes in prefrontal white matter post-mortem samples from a patient with schizophrenia (113). However, these microglial cells were described as “dystrophic”, while ultrastructural signs of oxidative stress, a feature of dark microglia, were not investigated in this study. To the best of our knowledge, this is the first time that dark microglia (i.e., microglia with a dense cyto- and- nucleoplasm and ultrastructural signs of oxidative stress) are reported in human post-mortem brain samples. The conservation of key features associated with dark microglia across mouse and human species, including an electron dense cyto- and nucleoplasm, altered mitochondria and dilated ER cisternae, along with several partially to fully-digested phagosomes, emphasizes the need to elucidate the mechanisms behind the appearance of this state and its role in AD.

Conclusion

Our ultrastructural investigation of microglial states in AD pathology revealed that dark microglia are preferentially distributed near A β and dystrophic neurites, appearing after these hallmarks emerge in the ventral hippocampus CA1 *stratum lacunosum-moleculare* of 20-month-old APP-PS1 and C57BL/6J male mice. The dark microglia interacted more with dystrophic neurites compared to typical microglia located near A β plaques and dystrophic neurites, and less with non-dystrophic axon terminals than typical microglia located far from A β plaques and dystrophic neurites. In addition, glycogen granules which are associated with a metabolic shift toward glycolysis were observed inside the cytoplasm of the typical

and especially dark microglia located near A β plaques and dystrophic neurites, highlighting the major impact these AD hallmarks have on the metabolism and intracellular content of these cells. It will be important in future studies to determine the functional outcome of this metabolic shift in dark microglia. Lastly, the dark microglia were observed in middle-aged and aged individuals, among post-mortem samples of the parahippocampal gyrus and hippocampal head, respectively, further identifying microglial ultrastructural similarities between mice and humans, and supporting the translational relevance of this investigation.

Abbreviations

AD Alzheimer's disease

AR aspect ratio

ATP adenosine triphosphate

ARM activated-response microglia

CNS central nervous system

CDM control dark microglia

CTM control typical microglia

DAM disease-associated microglia

DM dark microglia

E embryonic

ER endoplasmic reticulum

FDM dark microglia far from AD hallmarks

FTM typical microglia far from AD hallmarks

GWAS genome-wide association studies

Iba1 ionized calcium binding adaptor molecule 1

LOAD late-onset Alzheimer's disease

MgND microglial neurodegenerative phenotype

NDM dark microglia near AD hallmarks

NFT neurofibrillary tangles

NTM typical microglia near AD hallmarks

PAM plaque-associated microglia

PB phosphate buffer

PBS phosphate-buffered saline

PFKFB-3 6-phosphofructo-2-Kinase/Fructose-2,6-Biphosphate 3

SEM scanning electron microscope

TBS tris-buffered saline

TM typical microglia

Declarations

Ethical approval and consent to participate

All animal experiments were performed according to the guidelines of the Institutional Animal Ethics Committees, the Canadian Council on Animal Care, as well as the Animal Care Committee of Université Laval. Human post-mortem samples were obtained from the brain bank located at the CERVO Brain Research Center (QC, Canada). The brain bank and handling of the post-mortem human tissues were approved by the Ethics Committee of the Institut Universitaire en Santé Mentale de Québec and Université Laval. Written consent was obtained for the use of post-mortem tissues and all analyses were performed in line with the Code of Ethics of the World Medical Association.

Consent for publication

Not applicable.

Availability of data and material

All data presented in this study are available from the corresponding author upon reasonable request.

Competing interest

The authors declare that they have no competing interests.

Funding

MKSP is supported by doctoral training awards from the Canadian Institutes of Health Research (CIHR) and Fonds de recherche du Québec – Santé (FRQS). MC holds a FRQS doctoral's training award. ES is a

recipient of the Branch Out Foundation Graduate Grant and a Faculty of Graduate Studies (University of Victoria) Graduate Scholarships. MET holds a Canada Research Chair (Tier 2) in *Neurobiology of Aging and Cognition*. This work was funded by a CIHR Foundation grant (FDN341846) awarded to MET.

Author's contributions

MKSP and MET wrote the manuscript. MKSP conceived the figures. MKSP, FGI, MC and ES participated to the experiments. MJW, LV and MP provided the mice and human post-mortem samples. All the authors contributed to the article and approved the submitted version.

Acknowledgments

We acknowledge and respect that the University of Victoria is located on the territory of the lək̓ʷəŋən peoples and that the Songhees, Esquimalt, and WSÁNEĆ peoples have relationships to this land. We would like to thank Dr. Nathalie Vernoux and Hassan El Hajj for their help with the perfusion of the mice.

References

1. Spires-Jones TL, Hyman BT. The intersection of amyloid beta and tau at synapses in Alzheimer's disease. *Neuron*. 2014 May 21;82(4):756–71.
2. Terry RD, Masliah E, Salmon DP, Butters N, DeTeresa R, Hill R, et al. Physical basis of cognitive alterations in Alzheimer's disease: synapse loss is the major correlate of cognitive impairment. *Ann Neurol*. 1991 Oct;30(4):572–80.
3. Fjell AM, McEvoy L, Holland D, Dale AM, Walhovd KB, Alzheimer's Disease Neuroimaging Initiative. What is normal in normal aging? Effects of aging, amyloid and Alzheimer's disease on the cerebral cortex and the hippocampus. *Prog Neurobiol*. 2014 Jun;117:20–40.
4. Pini L, Pievani M, Bocchetta M, Altomare D, Bosco P, Cavedo E, et al. Brain atrophy in Alzheimer's Disease and aging. *Ageing Res Rev*. 2016 Sep;30:25–48.
5. Masurkar AV. Towards a circuit-level understanding of hippocampal CA1 dysfunction in Alzheimer's disease across anatomical axes. *J Alzheimers Dis Parkinsonism*. 2018;8(1):412.
6. Selles MC, Oliveira MM, Ferreira ST. Brain Inflammation Connects Cognitive and Non-Cognitive Symptoms in Alzheimer's Disease. *J Alzheimers Dis*. 2018;64(s1):S313–27.
7. Heneka MT, Carson MJ, El Khoury J, Landreth GE, Brosseron F, Feinstein DL, et al. Neuroinflammation in Alzheimer's Disease. *Lancet Neurol*. 2015 Apr;14(4):388–405.
8. Cabinio M, Saresella M, Piancone F, LaRosa F, Marventano I, Guerini FR, et al. Association between Hippocampal Shape, Neuroinflammation, and Cognitive Decline in Alzheimer's Disease. *J Alzheimers Dis*. 2018;66(3):1131–44.
9. Kinney JW, Bemiller SM, Murtishaw AS, Leisgang AM, Salazar AM, Lamb BT. Inflammation as a central mechanism in Alzheimer's disease. *Alzheimers Dement (N Y)*. 2018 Sep 6;4:575–90.

10. Hansen DV, Hanson JE, Sheng M. Microglia in Alzheimer's disease. *J Cell Biol.* 2018 Feb 5;217(2):459–72.
11. Sala Frigerio C, Wolfs L, Fattorelli N, Thrupp N, Voytyuk I, Schmidt I, et al. The Major Risk Factors for Alzheimer's Disease: Age, Sex, and Genes Modulate the Microglia Response to A β Plaques. *Cell Rep.* 2019 Apr 23;27(4):1293-1306.e6.
12. Sebastian Monasor L, Müller SA, Colombo AV, Tanriover G, König J, Roth S, et al. Fibrillar A β triggers microglial proteome alterations and dysfunction in Alzheimer mouse models. *Elife.* 2020 Jun 8;9:e54083.
13. Lodder C, Scheyltjens I, Stancu IC, Botella Lucena P, Gutiérrez de Ravé M, Vanherle S, et al. CSF1R inhibition rescues tau pathology and neurodegeneration in an A/T/N model with combined AD pathologies, while preserving plaque associated microglia. *Acta Neuropathologica Communications.* 2021 Jun 8;9(1):108.
14. Vogels T, Murgoci AN, Hromádka T. Intersection of pathological tau and microglia at the synapse. *Acta Neuropathologica Communications.* 2019 Jul 5;7(1):109.
15. Sosna J, Philipp S, Albay R, Reyes-Ruiz JM, Baglietto-Vargas D, LaFerla FM, et al. Early long-term administration of the CSF1R inhibitor PLX3397 ablates microglia and reduces accumulation of intraneuronal amyloid, neuritic plaque deposition and pre-fibrillar oligomers in 5XFAD mouse model of Alzheimer's disease. *Mol Neurodegener.* 2018 Mar 1;13(1):11.
16. Spangenberg E, Severson PL, Hohsfield LA, Crapser J, Zhang J, Burton EA, et al. Sustained microglial depletion with CSF1R inhibitor impairs parenchymal plaque development in an Alzheimer's disease model. *Nat Commun.* 2019 Aug 21;10(1):3758.
17. von Saucken VE, Jay TR, Landreth GE. The effect of amyloid on microglia-neuron interactions before plaque onset occurs independently of TREM2 in a mouse model of Alzheimer's disease. *Neurobiol Dis.* 2020 Nov;145:105072.
18. Ginhoux F, Greter M, Leboeuf M, Nandi S, See P, Gokhan S, et al. Fate mapping analysis reveals that adult microglia derive from primitive macrophages. *Science.* 2010 Nov 5;330(6005):841–5.
19. Andjelkovic AV, Nikolic B, Pachter JS, Zecevic N. Macrophages/microglial cells in human central nervous system during development: an immunohistochemical study. *Brain Res.* 1998 Dec 14;814(1–2):13–25.
20. Monier A, Evrard P, Gressens P, Verney C. Distribution and differentiation of microglia in the human encephalon during the first two trimesters of gestation. *J Comp Neurol.* 2006 Dec 1;499(4):565–82.
21. Verney C, Monier A, Fallet-Bianco C, Gressens P. Early microglial colonization of the human forebrain and possible involvement in periventricular white-matter injury of preterm infants. *J Anat.* 2010 Oct;217(4):436–48.
22. Tremblay MÈ, Stevens B, Sierra A, Wake H, Bessis A, Nimmerjahn A. The Role of Microglia in the Healthy Brain. *J Neurosci.* 2011 Nov 9;31(45):16064–9.
23. Šišková Z, Tremblay MÈ. Microglia and Synapse: Interactions in Health and Neurodegeneration. *Neural Plast [Internet].* 2013 [cited 2019 Dec 13];2013. Available from:

- <https://www.ncbi.nlm.nih.gov/pmc/articles/PMC3874338/>
24. Gomez-Nicola D, Perry VH. Microglial Dynamics and Role in the Healthy and Diseased Brain. *Neuroscientist*. 2015 Apr;21(2):169–84.
 25. Ransohoff RM, Khoury JE. Microglia in Health and Disease. *Cold Spring Harb Perspect Biol* [Internet]. 2016 Jan [cited 2019 Jan 29];8(1). Available from: <https://www.ncbi.nlm.nih.gov/pmc/articles/PMC4691795/>
 26. Augusto-Oliveira M, Arrifano GP, Lopes-Araújo A, Santos-Sacramento L, Takeda PY, Anthony DC, et al. What Do Microglia Really Do in Healthy Adult Brain? *Cells* [Internet]. 2019 Oct 22 [cited 2020 Jun 22];8(10). Available from: <https://www.ncbi.nlm.nih.gov/pmc/articles/PMC6829860/>
 27. Davalos D, Grutzendler J, Yang G, Kim JV, Zuo Y, Jung S, et al. ATP mediates rapid microglial response to local brain injury in vivo. *Nat Neurosci*. 2005 Jun;8(6):752–8.
 28. Nimmerjahn A, Kirchhoff F, Helmchen F. Resting microglial cells are highly dynamic surveillants of brain parenchyma in vivo. *Science*. 2005 May 27;308(5726):1314–8.
 29. Parkhurst CN, Yang G, Ninan I, Savas JN, Yates JR, Lafaille JJ, et al. Microglia promote learning-dependent synapse formation through BDNF. *Cell*. 2013 Dec 19;155(7):1596–609.
 30. Weinhard L, di Bartolomei G, Bolasco G, Machado P, Schieber NL, Neniskyte U, et al. Microglia remodel synapses by presynaptic trogocytosis and spine head filopodia induction. *Nat Commun*. 2018 26;9(1):1228.
 31. Tremblay MÈ, Majewska AK. A role for microglia in synaptic plasticity? *Commun Integr Biol*. 2011 Mar;4(2):220–2.
 32. Bliss TVP, Collingridge GL, Morris RGM. Synaptic plasticity in health and disease: introduction and overview. *Philos Trans R Soc Lond B Biol Sci* [Internet]. 2014 Jan 5 [cited 2019 Jan 29];369(1633). Available from: <https://www.ncbi.nlm.nih.gov/pmc/articles/PMC3843863/>
 33. Hong S, Dissing-Olesen L, Stevens B. New insights on the role of microglia in synaptic pruning in health and disease. *Curr Opin Neurobiol*. 2016 Feb;36:128–34.
 34. Paolicelli R, Sierra A, Stevens B, Tremblay ME, Aguzzi A, Ajami B, et al. Defining Microglial States and Nomenclature: A Roadmap to 2030 [Internet]. Rochester, NY: Social Science Research Network; 2022 Mar [cited 2022 May 4]. Report No.: 4065080. Available from: <https://papers.ssrn.com/abstract=4065080>
 35. Streit WJ, Sammons NW, Kuhns AJ, Sparks DL. Dystrophic microglia in the aging human brain. *Glia*. 2004 Jan 15;45(2):208–12.
 36. Streit WJ, Braak H, Xue QS, Bechmann I. Dystrophic (senescent) rather than activated microglial cells are associated with tau pathology and likely precede neurodegeneration in Alzheimer’s disease. *Acta Neuropathol*. 2009 Oct;118(4):475–85.
 37. Streit WJ, Khoshbouei H, Bechmann I. Dystrophic microglia in late-onset Alzheimer’s disease. *Glia*. 2020 Apr;68(4):845–54.

38. Lopes KO, Sparks DL, Streit WJ. Microglial dystrophy in the aged and Alzheimer's disease brain is associated with ferritin immunoreactivity. *Glia*. 2008 Aug 1;56(10):1048–60.
39. Swanson MEV, Murray HC, Ryan B, Faull RLM, Dragunow M, Curtis MA. Quantitative immunohistochemical analysis of myeloid cell marker expression in human cortex captures microglia heterogeneity with anatomical context. *Sci Rep*. 2020 Jul 16;10(1):11693.
40. Yuan P, Condello C, Keene CD, Wang Y, Bird TD, Paul SM, et al. TREM2 Haplodeficiency in Mice and Humans Impairs the Microglia Barrier Function Leading to Decreased Amyloid Compaction and Severe Axonal Dystrophy. *Neuron*. 2016 May 18;90(4):724–39.
41. Yin Z, Raj D, Saiepour N, Van Dam D, Brouwer N, Holtman IR, et al. Immune hyperreactivity of A β plaque-associated microglia in Alzheimer's disease. *Neurobiol Aging*. 2017 Jul;55:115–22.
42. Condello C, Yuan P, Grutzendler J. Microglia-Mediated Neuroprotection, TREM2, and Alzheimer's Disease: Evidence From Optical Imaging. *Biol Psychiatry*. 2018 Feb 15;83(4):377–87.
43. Hashemiaghdam A, Mroczek M. Microglia heterogeneity and neurodegeneration: The emerging paradigm of the role of immunity in Alzheimer's disease. *J Neuroimmunol*. 2020 Apr 15;341:577185.
44. Grubman A, Choo XY, Chew G, Ouyang JF, Sun G, Croft NP, et al. Transcriptional signature in microglia associated with A β plaque phagocytosis. *Nat Commun*. 2021 May 21;12(1):3015.
45. Michaud JP, Bellavance MA, Préfontaine P, Rivest S. Real-Time In Vivo Imaging Reveals the Ability of Monocytes to Clear Vascular Amyloid Beta. *Cell Reports*. 2013 Nov 14;5(3):646–53.
46. Rivera-Escalera F, Pinney JJ, Owlett L, Ahmed H, Thakar J, Olschowka JA, et al. IL-1 β -driven amyloid plaque clearance is associated with an expansion of transcriptionally reprogrammed microglia. *J Neuroinflammation*. 2019 Dec 10;16(1):261.
47. Casali BT, MacPherson KP, Reed-Geaghan EG, Landreth GE. Microglia depletion rapidly and reversibly alters amyloid pathology by modification of plaque compaction and morphologies. *Neurobiol Dis*. 2020 Aug;142:104956.
48. Huang Y, Happonen KE, Burrola PG, O'Connor C, Hah N, Huang L, et al. Microglia use TAM receptors to detect and engulf amyloid β plaques. *Nat Immunol*. 2021 May;22(5):586–94.
49. Daria A, Colombo A, Llovera G, Hampel H, Willem M, Liesz A, et al. Young microglia restore amyloid plaque clearance of aged microglia. *EMBO J*. 2017 Mar 1;36(5):583–603.
50. Koellhoffer EC, McCullough LD, Ritzel RM. Old Maids: Aging and Its Impact on Microglia Function. *Int J Mol Sci*. 2017 Apr 5;18(4):E769.
51. Kaur D, Sharma V, Deshmukh R. Activation of microglia and astrocytes: a roadway to neuroinflammation and Alzheimer's disease. *Inflammopharmacology*. 2019 Aug;27(4):663–77.
52. Yuan C, Aierken A, Xie Z, Li N, Zhao J, Qing H. The age-related microglial transformation in Alzheimer's disease pathogenesis. *Neurobiol Aging*. 2020 Aug;92:82–91.
53. Edler MK, Mhatre-Winters I, Richardson JR. Microglia in Aging and Alzheimer's Disease: A Comparative Species Review. *Cells*. 2021 May 8;10(5):1138.

54. Baik SH, Kang S, Lee W, Choi H, Chung S, Kim JI, et al. A Breakdown in Metabolic Reprogramming Causes Microglia Dysfunction in Alzheimer's Disease. *Cell Metab.* 2019 Sep 3;30(3):493-507.e6.
55. McIntosh A, Mela V, Harty C, Minogue AM, Costello DA, Kerskens C, et al. Iron accumulation in microglia triggers a cascade of events that leads to altered metabolism and compromised function in APP/PS1 mice. *Brain Pathol.* 2019 Sep;29(5):606–21.
56. Guillot-Sestier MV, Araiz AR, Mela V, Gaban AS, O'Neill E, Joshi L, et al. Microglial metabolism is a pivotal factor in sexual dimorphism in Alzheimer's disease. *Commun Biol.* 2021 Jun 10;4(1):711.
57. Holland R, McIntosh AL, Finucane OM, Mela V, Rubio-Araiz A, Timmons G, et al. Inflammatory microglia are glycolytic and iron retentive and typify the microglia in APP/PS1 mice. *Brain Behav Immun.* 2018 Feb;68:183–96.
58. Shibuya T, Tsujimoto Y. Deleterious effects of mitochondrial ROS generated by KillerRed photodynamic action in human cell lines and *C. elegans*. *J Photochem Photobiol B.* 2012 Dec 5;117:1–12.
59. Guo C, Sun L, Chen X, Zhang D. Oxidative stress, mitochondrial damage and neurodegenerative diseases. *Neural Regen Res.* 2013 Jul 25;8(21):2003–14.
60. Zeeshan HMA, Lee GH, Kim HR, Chae HJ. Endoplasmic Reticulum Stress and Associated ROS. *Int J Mol Sci.* 2016 Mar 2;17(3):327.
61. Minhas PS, Latif-Hernandez A, McReynolds MR, Durairaj AS, Wang Q, Rubin A, et al. Restoring metabolism of myeloid cells reverses cognitive decline in ageing. *Nature.* 2021 Feb;590(7844):122–8.
62. Keren-Shaul H, Spinrad A, Weiner A, Matcovitch-Natan O, Dvir-Szternfeld R, Ulland TK, et al. A Unique Microglia Type Associated with Restricting Development of Alzheimer's Disease. *Cell.* 2017 Jun 15;169(7):1276-1290.e17.
63. Krasemann S, Madore C, Cialic R, Baufeld C, Calcagno N, El Fatimy R, et al. The TREM2-APOE Pathway Drives the Transcriptional Phenotype of Dysfunctional Microglia in Neurodegenerative Diseases. *Immunity.* 2017 19;47(3):566-581.e9.
64. Bisht K, Sharma KP, Lecours C, Gabriela Sánchez M, El Hajj H, Milior G, et al. Dark microglia: A new phenotype predominantly associated with pathological states. *Glia.* 2016 May;64(5):826–39.
65. El Hajj H, Savage JC, Bisht K, Parent M, Vallières L, Rivest S, et al. Ultrastructural evidence of microglial heterogeneity in Alzheimer's disease amyloid pathology. *J Neuroinflammation.* 2019 Apr 16;16(1):87.
66. Stratoulis V, Venero JL, Tremblay MÈ, Joseph B. Microglial subtypes: diversity within the microglial community. *EMBO J.* 2019 Sep 2;38(17):e101997.
67. Jankowsky JL, Zheng H. Practical considerations for choosing a mouse model of Alzheimer's disease. *Mol Neurodegener.* 2017 Dec 22;12(1):89.
68. Pozueta J, Lefort R, Shelanski ML. Synaptic changes in Alzheimer's disease and its models. *Neuroscience.* 2013 Oct 22;251:51–65.

69. Janota CS, Brites D, Lemere CA, Brito MA. Glio-vascular changes during ageing in wild-type and Alzheimer's disease-like APP/PS1 mice. *Brain Res.* 2015 Sep 16;1620:153–68.
70. Jackson SJ, Andrews N, Ball D, Bellantuono I, Gray J, Hachoumi L, et al. Does age matter? The impact of rodent age on study outcomes. *Lab Anim.* 2017 Apr;51(2):160–9.
71. Koizumi J. Glycogen in the central nervous system. *Prog Histochem Cytochem.* 1974;6(4):1–37.
72. Hirase H, Akther S, Wang X, Oe Y. Glycogen distribution in mouse hippocampus. *J Neurosci Res.* 2019 Aug;97(8):923–32.
73. Borchelt DR, Ratovitski T, van Lare J, Lee MK, Gonzales V, Jenkins NA, et al. Accelerated amyloid deposition in the brains of transgenic mice coexpressing mutant presenilin 1 and amyloid precursor proteins. *Neuron.* 1997 Oct;19(4):939–45.
74. Mielke MM. Sex and Gender Differences in Alzheimer's Disease Dementia. *Psychiatr Times.* 2018 Nov;35(11):14–7.
75. Bisht K, El Hajj H, Savage JC, Sánchez MG, Tremblay MÈ. Correlative Light and Electron Microscopy to Study Microglial Interactions with β -Amyloid Plaques. *J Vis Exp.* 2016 Jun 1;(112).
76. St-Pierre MK, Bordeleau M, Tremblay MÈ. Visualizing Dark Microglia. *Methods Mol Biol.* 2019;2034:97–110.
77. St-Pierre MK, Carrier M, Lau V, Tremblay MÈ. Investigating Microglial Ultrastructural Alterations and Intimate Relationships with Neuronal Stress, Dystrophy, and Degeneration in Mouse Models of Alzheimer's Disease. In: *Neuronal Cell Death.* In press.
78. St-Pierre MK, Šimončičová E, Bögi E, Tremblay MÈ. Shedding Light on the Dark Side of the Microglia. *ASN Neuro [Internet].* 2020 May 22 [cited 2020 Jun 25];12. Available from: <https://www.ncbi.nlm.nih.gov/pmc/articles/PMC7249604/>
79. Bordeleau M, Lacabanne C, Fernández de Cossío L, Vernoux N, Savage JC, González-Ibáñez F, et al. Microglial and peripheral immune priming is partially sexually dimorphic in adolescent mouse offspring exposed to maternal high-fat diet. *Journal of Neuroinflammation.* 2020 Sep 5;17(1):264.
80. Serdar CC, Cihan M, Yücel D, Serdar MA. Sample size, power and effect size revisited: simplified and practical approaches in pre-clinical, clinical and laboratory studies. *Biochem Med (Zagreb).* 2021 Feb 15;31(1):010502.
81. Nahirney PC, Tremblay ME. Brain Ultrastructure: Putting the Pieces Together. *Front Cell Dev Biol [Internet].* 2021 [cited 2021 Feb 24];9. Available from: <https://www.frontiersin.org/articles/10.3389/fcell.2021.629503/full>
82. Lecours C, St-Pierre MK, Picard K, Bordeleau M, Bourque M, Awogbindin IO, et al. Levodopa partially rescues microglial numerical, morphological, and phagolysosomal alterations in a monkey model of Parkinson's disease. *Brain Behav Immun.* 2020 Nov;90:81–96.
83. Peters A, Palay SL, Webster H deF. The fine structure of the nervous system: neurons and their supporting cells. Oxford University Press; 1991. 534 p.

84. Frackowiak J, Wisniewski HM, Wegiel J, Merz GS, Iqbal K, Wang KC. Ultrastructure of the microglia that phagocytose amyloid and the microglia that produce beta-amyloid fibrils. *Acta Neuropathol.* 1992;84(3):225–33.
85. Stalder M, Phinney A, Probst A, Sommer B, Staufenbiel M, Jucker M. Association of microglia with amyloid plaques in brains of APP23 transgenic mice. *Am J Pathol.* 1999 Jun;154(6):1673–84.
86. Bordeleau M, Fernández de Cossío L, Lacabanne C, Savage JC, Vernoux N, Chakravarty M, et al. Maternal high-fat diet modifies myelin organization, microglial interactions, and results in social memory and sensorimotor gating deficits in adolescent mouse offspring. *Brain, Behavior, & Immunity - Health.* 2021 Aug 1;15:100281.
87. Tremblay MÈ, Zettel ML, Ison JR, Allen PD, Majewska AK. Effects of aging and sensory loss on glial cells in mouse visual and auditory cortices. *Glia.* 2012;60(4):541–58.
88. Tremblay MÈ, Majewska AK. Ultrastructural Analyses of Microglial Interactions with Synapses. *Methods Mol Biol.* 2019;2034:83–95.
89. Mondo E, Becker SC, Kautzman AG, Schifferer M, Baer CE, Chen J, et al. A Developmental Analysis of Juxtavascular Microglia Dynamics and Interactions with the Vasculature. *J Neurosci.* 2020 Aug 19;40(34):6503–21.
90. Hui CW, St-Pierre MK, Detuncq J, Aumailley L, Dubois MJ, Couture V, et al. Nonfunctional mutant Wrn protein leads to neurological deficits, neuronal stress, microglial alteration, and immune imbalance in a mouse model of Werner syndrome. *Brain, Behavior, and Immunity.* 2018 Oct 1;73:450–69.
91. Prats C, Graham TE, Shearer J. The dynamic life of the glycogen granule. *J Biol Chem.* 2018 May 11;293(19):7089–98.
92. Hart ML, Lauer JC, Selig M, Hanak M, Walters B, Rolauffs B. Shaping the Cell and the Future: Recent Advancements in Biophysical Aspects Relevant to Regenerative Medicine. *Journal of Functional Morphology and Kinesiology.* 2018 Mar;3(1):2.
93. Leyh J, Paeschke S, Mages B, Michalski D, Nowicki M, Bechmann I, et al. Classification of Microglial Morphological Phenotypes Using Machine Learning. *Frontiers in Cellular Neuroscience.* 2021;15:241.
94. Savage JC, St-Pierre MK, Carrier M, El Hajj H, Novak SW, Sanchez MG, et al. Microglial physiological properties and interactions with synapses are altered at presymptomatic stages in a mouse model of Huntington’s disease pathology. *J Neuroinflammation [Internet].* 2020 Apr 2 [cited 2020 Apr 13];17. Available from: <https://www.ncbi.nlm.nih.gov/pmc/articles/PMC7118932/>
95. Yasumoto Y, Stoiljkovic M, Kim JD, Sestan-Pesa M, Gao XB, Diano S, et al. Ucp2-dependent microglia-neuronal coupling controls ventral hippocampal circuit function and anxiety-like behavior. *Mol Psychiatry.* 2021 Jul;26(7):2740–52.
96. Hou Y, Dan X, Babbar M, Wei Y, Hasselbalch SG, Croteau DL, et al. Ageing as a risk factor for neurodegenerative disease. *Nat Rev Neurol.* 2019 Oct;15(10):565–81.
97. Šišková Z, Justus D, Kaneko H, Friedrichs D, Henneberg N, Beutel T, et al. Dendritic structural degeneration is functionally linked to cellular hyperexcitability in a mouse model of Alzheimer’s disease. *Neuron.* 2014 Dec 3;84(5):1023–33.

98. Sanchez-Varo R, Sanchez-Mejias E, Fernandez-Valenzuela JJ, De Castro V, Mejias-Ortega M, Gomez-Arboledas A, et al. Plaque-Associated Oligomeric Amyloid-Beta Drives Early Synaptotoxicity in APP/PS1 Mice Hippocampus: Ultrastructural Pathology Analysis. *Frontiers in Neuroscience* [Internet]. 2021 [cited 2022 May 9];15. Available from: <https://www.frontiersin.org/article/10.3389/fnins.2021.752594>
99. Unger MS, Marschallinger J, Kaindl J, Höfling C, Rossner S, Heneka MT, et al. Early Changes in Hippocampal Neurogenesis in Transgenic Mouse Models for Alzheimer's Disease. *Mol Neurobiol*. 2016 Oct;53(8):5796–806.
100. Nasrabady SE, Rizvi B, Goldman JE, Brickman AM. White matter changes in Alzheimer's disease: a focus on myelin and oligodendrocytes. *Acta Neuropathologica Communications*. 2018 Mar 2;6(1):22.
101. Acharjee S, Verbeek M, Gomez CD, Bisht K, Lee B, Benoit L, et al. Reduced Microglial Activity and Enhanced Glutamate Transmission in the Basolateral Amygdala in Early CNS Autoimmunity. *J Neurosci*. 2018 Oct 17;38(42):9019–33.
102. Garofalo S, Porzia A, Mainiero F, Di Angelantonio S, Cortese B, Basilico B, et al. Environmental stimuli shape microglial plasticity in glioma. *Elife*. 2017 Dec 29;6:e33415.
103. Alvarez-Vergara MI, Rosales-Nieves AE, March-Diaz R, Rodriguez-Perinan G, Lara-Ureña N, Ortega-de San Luis C, et al. Non-productive angiogenesis disassembles A β plaque-associated blood vessels. *Nat Commun*. 2021 May 25;12:3098.
104. Oe Y, Baba O, Ashida H, Nakamura KC, Hirase H. Glycogen distribution in the microwave-fixed mouse brain reveals heterogeneous astrocytic patterns. *Glia*. 2016 Sep;64(9):1532–45.
105. Guma E, Bordeleau M, González Ibáñez F, Picard K, Snook E, Desrosiers-Grégoire G, et al. Differential effects of early or late exposure to prenatal maternal immune activation on mouse embryonic neurodevelopment. *Proc Natl Acad Sci U S A*. 2022 Mar 22;119(12):e2114545119.
106. Hui CW, St-Pierre A, El Hajj H, Remy Y, Hébert SS, Luheshi GN, et al. Prenatal Immune Challenge in Mice Leads to Partly Sex-Dependent Behavioral, Microglial, and Molecular Abnormalities Associated with Schizophrenia. *Front Mol Neurosci*. 2018;11:13.
107. Rizou SV, Evangelou K, Myrianthopoulos V, Mourouzis I, Havaki S, Athanasiou A, et al. A Novel Quantitative Method for the Detection of Lipofuscin, the Main By-Product of Cellular Senescence, in Fluids. *Methods Mol Biol*. 2019;1896:119–38.
108. Clayton K, Delpech JC, Herron S, Iwahara N, Ericsson M, Saito T, et al. Plaque associated microglia hyper-secrete extracellular vesicles and accelerate tau propagation in a humanized APP mouse model. *Molecular Neurodegeneration*. 2021 Mar 22;16(1):18.
109. Gyoneva S, Swanger SA, Zhang J, Weinshenker D, Traynelis SF. Altered motility of plaque-associated microglia in a model of Alzheimer's disease. *Neuroscience*. 2016 Aug 25;330:410–20.
110. Shukla AK, McIntyre LL, Marsh SE, Schneider CA, Hoover EM, Walsh CM, et al. CD11a expression distinguishes infiltrating myeloid cells from plaque-associated microglia in Alzheimer's disease. *Glia*. 2019 May;67(5):844–56.

111. Gomez-Arboledas A, Davila JC, Sanchez-Mejias E, Navarro V, Nuñez-Diaz C, Sanchez-Varo R, et al. Phagocytic clearance of presynaptic dystrophies by reactive astrocytes in Alzheimer's disease. *Glia*. 2018 Mar;66(3):637–53.
112. Zeineh MM, Chen Y, Kitzler HH, Hammond R, Vogel H, Rutt BK. Activated iron-containing microglia in the human hippocampus identified by magnetic resonance imaging in Alzheimer disease. *Neurobiol Aging*. 2015 Sep;36(9):2483–500.
113. Uranova NA, Vikhрева OV, Rakhmanova VI, Orlovskaya DD. Ultrastructural pathology of oligodendrocytes adjacent to microglia in prefrontal white matter in schizophrenia. *NPJ Schizophr*. 2018 Dec 13;4(1):26.

Tables

Table 1

Ultrastructural analysis of microglia categorized based on their proximity to A β plaques and dystrophic neurites as well as cellular state in the ventral hippocampus CA1 *stratum lacunosum-moleculare* of aged C56BL/6J and APP-PS1 male mice

	CTM Mean ± SEM	FTM Mean ± SEM	NTM Mean ± SEM	NDM Mean ± SEM
Area (µm ²)	26.54 ± 1.702	28.20 ± 1.859	27.96 ± 2.094	26.76 ± 1.678
Perimeter (µm)	25.25 ± 1.437	24.54 ± 1.221	25.71 ± 1.837	32.49 ± 3.204
Circularity (a.u)	0.5545 ± 0.02709	0.5993 ± 0.02212	0.5820 ± 0.03226	0.4417 ± 0.03181
Aspect ratio (a.u)	1.732 ± 0.08945	1.522 ± 0.07346	1.716 ± 0.1092	1.992 ± 0.1596
Roundness (a.u)	0.6175 ± 0.03100	0.6942 ± 0.02864	0.6386 ± 0.03525	0.5690 ± 0.03428
Solidness (a.u)	0.8670 ± 0.01766	0.8891 ± 0.01269	0.8620 ± 0.02242	0.8038 ± 0.02264
Associations with vasculature (n)	0.3333 ± 0.09245	0.006897 ± 0.04789	0.03704 ± 0.03704	0.03571 ± 0.03571
Associations with myelinated axons (n)	0.556 ± 0.1716	0.6207 ± 0.1818	0.2593 ± 0.1653	0.0 ± 0.0
Axon terminals (n)	4.926 ± 0.7059	6.207 ± 0.5490	5.074 ± 0.5493	4.107 ± 0.4581
Dendritic spines (n)	0.4444 ± 0.1541	1.103 ± 0.2866	0.8889 ± 0.1631	0.4643 ± 0.1204
Synaptic clefts (n)	1.074 ± 0.2611	1.138 ± 0.2089	1.148 ± 0.1826	0.8571 ± 0.2557
All synaptic contacts (n)	6.444 ± 0.8136	8.448 ± 0.6250	7.1111 ± 0.6300	5.429 ± 0.4945
Primary lysosomes (n)	0.0 ± 0.0	0.03448 ± 0.03448	0.07407 ± 0.05136	0.07143 ± 0.04956
Secondary lysosomes (n)	0.03704 ± 0.03704	0.1034 ± 0.05755	0.444 ± 0.1631	0.3214 ± 0.1265
Tertiary lysosomes (n)	0.5556 ± 0.1445	0.2069 ± 0.07655	0.1852 ± 0.09302	0.3571 ± 0.1282
All lysosomes (n)	0.6296 ± 0.1614	0.3448 ± 0.08983	0.7937 ± 0.2123	0.7500 ± 0.1677
Lipid bodies (n)	1.074 ± 0.2383	0.7586 ± 0.2748	0.7037 ± 0.3493	0.8929 ± 0.3386
Lipofuscin granules (n)	0.8148 ± 0.1927	0.6897 ± 0.1929	1.000 ± 0.3849	0.9286 ± 0.2116
Partially digested endosomes (n)	0.5185 ± 0.1449	0.9310 ± 0.2216	1.44 ± 0.3261	1.250 ± 0.3155

Fully digested endosomes (n)	0.3333 ± 0.1688	0.7931 ± 0.1674	0.7407 ± 0.2480	0.9643 ± 0.2976
All endosomes (n)	0.7407 ± 0.2174	1.759 ± 0.2836	2.185 ± 0.4685	2.214 ± 0.4780
Autophagosomes (n)	0.2222 ± 0.09745	0.06897 ± 0.04789	0.2222 ± 0.1111	0.3571 ± 0.1282
Fibrillar materials (n)	0.0 ± 0.0	0.06897 ± 0.04789	0.1111 ± 0.06163	0.07143 ± 0.04956
Altered mitochondria (n)	0.3704 ± 0.1087	1.207 ± 0.1815	1.889 ± 0.4347	3.464 ± 0.6289
Elongated mitochondria (n)	0.3333 ± 0.1194	0.4138 ± 0.1267	0.4074 ± 0.1710	0.6071 ± 0.2376
Dilated ER/Golgi apparatus (n)	0.2222 ± 0.1111	0.5862 ± 0.1955	1.593 ± 0.3968	2.071 ± 0.4740

CTM control typical microglia, FTM typical microglia far from amyloid beta plaque and dystrophic neurites, NTM typical microglia near amyloid beta plaque and dystrophic neurite, NDM dark microglia near amyloid beta plaque and dystrophic neurite, n number, a.u. arbitrary unit, ER endoplasmic reticulum, P-values of statistically significant tests are highlighted in bold.

Table 2

Relative percentage of the ultrastructural analysis of microglia categorized based on their proximity to A β plaques and dystrophic neurites as well as cellular state in the ventral hippocampus CA1 *stratum lacunosum-moleculare* of aged C56BL/6J and APP-PS1 male mice

	CTM Mean ± SEM	FTM Mean ± SEM	NTM Mean ± SEM	NDM Mean ± SEM
Associations with myelinated axons (%)	33.33 ± 9.245	37.93 ± 9.170	11.11 ± 6.163	0.0 ± 0.0
Extracellular space (%)	25.93 ± 8.594	51.72 ± 9.443	14.81 ± 6.967	21.43 ± 7.897
Extracellular digestion (%)	25.93 ± 8.594	17.24 ± 7.139	14.81 ± 6.967	7.143 ± 4.956
Primary lysosomes (%)	0.0 ± 0.0	3.448 ± 3.448	7.407 ± 5.136	7.143 ± 4.956
Secondary lysosomes (%)	3.704 ± 3.704	10.34 ± 5.755	18.59 ± 7.611	21.43 ± 7.897
Tertiary lysosomes (%)	44.44 ± 9.745	20.69 ± 7.655	14.81 ± 6.967	25.00 ± 8.333
All lysosomes (%)	44.44 ± 9.745	34.48 ± 8.983	37.04 ± 9.471	50.00 ± 9.623
Lipid bodies (%)	55.56 ± 9.745	34.48 ± 8.983	29.63 ± 8.955	32.14 ± 8.988
Lipofuscin granules (%)	44.44 ± 9.745	37.93 ± 9.170	29.63 ± 8.955	50.00 ± 9.623
Partially digested endosomes (%)	37.04 ± 9.471	48.28 ± 9.443	55.56 ± 9.745	57.14 ± 9.524
Fully digested endosomes (%)	18.52 ± 7.618	51.72 ± 9.443	33.33 ± 9.245	50.00 ± 9.623
All endosomes (%)	40.74 ± 9.636	72.41 ± 8.447	59.26 ± 9.636	67.86 ± 8.988
Autophagosomes (%)	18.52 ± 7.618	6.897 ± 4.789	14.81 ± 6.967	28.57 ± 8.694
Altered mitochondria (%)	33.33 ± 9.245	72.41 ± 8.447	70.37 ± 8.955	78.57 ± 7.897
Elongated mitochondria (%)	25.93 ± 8.594	31.03 ± 8.743	22.22 ± 8.153	32.14 ± 8.988
Dilated ER/Golgi apparatus (%)	14.81 ± 6.967	37.93 ± 9.170	55.56 ± 9.745	60.71 ± 9.399
Glycogen granules (%)	0.000 ± 0.000	3.448 ± 3.448	29.63 ± 8.955	60.71 ± 9.399

CTM control typical microglia, FTM typical microglia far from amyloid beta plaque and dystrophic neurite, NTM typical microglia near amyloid beta plaque and dystrophic neurite, NDM dark microglia near amyloid beta plaque and dystrophic neurite, % percentage, a.u. arbitrary unit, ER endoplasmic reticulum, P-values of statistically significant tests are highlighted in bold.

Figures

Figure 1

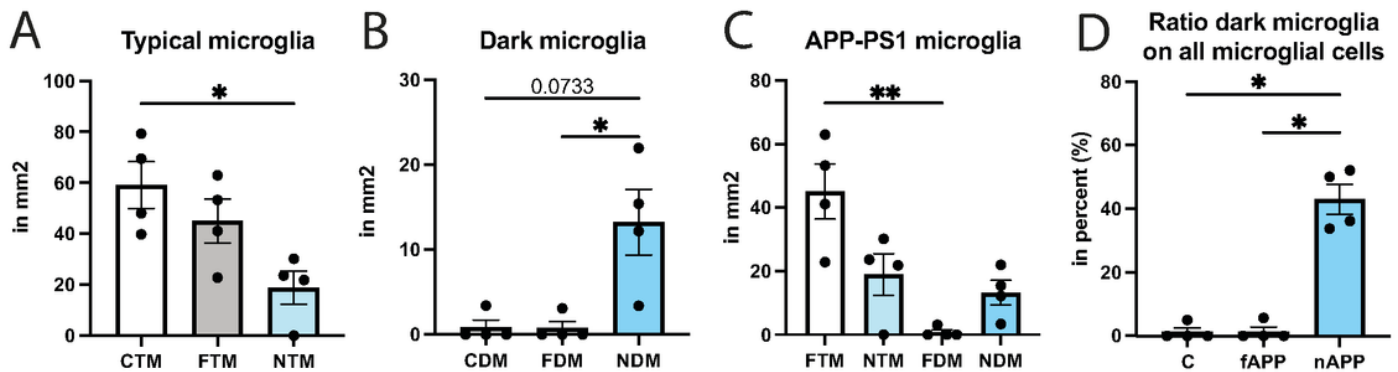


Figure 1

Distribution and density of dark vs typical microglia.

Density analysis based on ultrastructural characteristics of dark (DM) and typical microglia (TM) in the ventral hippocampus CA1 *stratum lacunosum-moleculare* of 20-month-old and age-matched C57BL/6J male mice. The density of TM (A) and DM (B) is shown. The density of microglia based on their proximity to plaques (far or near) as well as their state (TM or DM) is provided (C). The percentage of DM over all the microglia far from plaques or near plaques is represented in (D). Data shown are expressed as means \pm S.E.M. * $p < 0.05$, ** $p < 0.01$, using a Kruskal-Wallis test with Dunn's multiple comparisons test. $n = 4$ animals.

Figure 2

Dark vs typical microglia's interactions with dystrophic neurites and A β plaques.

Representative 5 nm resolution scanning electron microscopy images captured in the ventral hippocampus CA1 *stratum lacunosum-moleculare* of 20-month-old APP-PS1 male mice. (A) Typical

microglia (TM) observed near extracellular fibrillar A β (pseudocolored in purple) and dystrophic neurites (pseudocolored in pink). (B) Dark microglia (DM) interacting with several dystrophic neurites along with fibrillar A β . (C-F) Quantitative graphs representing the numbers of contacts with dystrophic neurite (C) and A β plaques (D) as well as the proportion of microglial cells contacting dystrophic neurites (E) or A β plaques (F). Data shown are expressed as means \pm S.E.M. * $p < 0.05$, ** $p < 0.01$, using a non-parametric unpaired Student's t-test. $n = 9-12$ microglia per animal, in $N = 3$ mice/group. Purple = fibrillar A β , pink = dystrophic neurites, red outline = plasma membrane, yellow outline = nuclear membrane.

Figure 3

Dark vs typical microglia's interactions with parenchymal elements.

Representative 5 nm resolution scanning electron microscopy images taken in the ventral hippocampus CA1 *stratum lacunosum-moleculare* of 20-month-old APP-PS1 and C57BL/6J male mice. (A) Typical microglia (TM) in C57BL/6J mice contacting a blood vessel (BV) and myelinated axons (pseudocolored in yellow) as well as axon terminals (pseudocolored in blue), (B) TM far from a plaque interacting with axon terminals and dendritic spines (pseudocolored in orange) which are associated with extracellular space pockets (pseudocolored in lilac), (C) TM near a plaque interacting with a few axon terminals, (D) dark microglia (DM) near a plaque is contacting axon terminals. Graphs representing the number of axon terminals (E), all synaptic interactions (F), percentage of cells associating with the vasculature (G), myelinated axons (F), as well as the percentage of cells touching a myelinated axon (J). Data shown are expressed as means \pm S.E.M. * $p < 0.05$, ** $p < 0.01$, using a Kruskal-Wallis test with a Dunn's multiple comparisons test. $n = 9-12$ microglia per animal, in $N = 3$ mice/group. Red outline = plasma membrane, yellow outline = nuclear membrane, blue outline = basement membrane.

Figure 4

Shape descriptors of dark vs typical microglia.

Representative 5 nm resolution scanning electron microscopy images captured in the ventral hippocampus CA1 *stratum lacunosum-moleculare* of 20-month-old APP-PS1 and C57BL/6J male mice. (A) typical microglia (TM) in C57BL/6J mice, (B) TM far from A β plaque, (C) TM near A β plaques and dystrophic neurites, (D) dark microglia (DM) near A β plaques and dystrophic neurites in APP-PS1 mice. (E-I) Graphs representing the shape descriptors of microglia: (E) area, (F) perimeter, (G) circularity, (H) aspect ratio and (I) solidity. Data shown are expressed as means \pm S.E.M. * $p < 0.05$, ** $p < 0.01$, using a

Kruskal-Wallis test with Dunn's multiple comparisons test. n = 9–12 microglia per animal, in N = 3 mice/group. Red outline = plasma membrane, yellow outline = nuclear membrane.

Figure 5

Ultrastructural signs of cellular stress in dark vs typical microglia.

Representative 5 nm resolution scanning electron microscopy images taken in the ventral hippocampus CA1 *stratum lacunosum-moleculare* of 20-month-old APP-PS1 and C57BL/6J male mice. (A) Typical microglia (TM) in C57BL/6J mice without visible ultrastructural signs of cellular stress, (B) TM far from a plaque with altered mitochondria (pseudocolored in blue) (C) TM near a plaque with healthy endoplasmic reticulum cisternae (pseudocolored in orange), (D) dark microglia (DM) near a plaque with altered mitochondria, healthy and dilated endoplasmic reticulum cisternae (pseudocolored in green) in APP-PS1 mice. Graphs representing the number and proportion of microglial cells with dilated endoplasmic reticulum and/or Golgi apparatus cisternae (E, H), altered mitochondria (F, I) and elongated mitochondria (G, J) are presented. Data shown are expressed as means \pm S.E.M. * p < 0.05, ** p < 0.01, **** p < 0.001 using a Kruskal-Wallis test with a Dunn's multiple comparisons test. n = 9–12 microglia per animal, in N = 3 mice/group. Red outline = plasma membrane, yellow outline = nuclear membrane.

Figure 6

Glycogen granules in the cytoplasm of dark vs typical microglia.

Representative 5 nm resolution scanning electron microscopy images captured in the ventral hippocampus CA1 *stratum lacunosum-moleculare* of 20-month-old APP-PS1 male mice. (A) Typical microglia (TM) near extracellular fibrillar A β (NTM) and (C) dark microglia (DM) near A β (NDM), both presenting glycogen granules in their cytoplasm (white arrow). B-D represent the insets of A and C, respectively. (E) Graph representing the proportion of microglia positive for glycogen granules. Data shown are expressed as means \pm S.E.M. * p < 0.05, **** p < 0.001 using a Kruskal-Wallis test with a Dunn's multiple comparisons test. n = 9–12 cells per animal, in N = 3 mice/group. Red outline = plasma membrane, yellow outline = nuclear membrane.

Figure 7

Dark vs typical microglia in aging human post-mortem brain samples.

Representative 5 nm resolution scanning electron microscopy images in human post-mortem hippocampal head (post-mortem delay of 18 h) of (A) a 45-year old man and (B) a 81-year old woman. (A) Typical microglia (TM) positive for the myeloid cell marker Iba1 with healthy and altered mitochondria located next to a DM. The insets provide a zoom in view of the (B) TM and (C) DM. (D) TM with lysosomes (pseudocolored in blue) and mitochondria (pseudocolored in purple) next to a DM displaying altered mitochondria, empty phagosomes (pseudocolored in cyan) and phagosomes with cellular contents (pseudocolored in pink). The insets provide a higher magnification of the (E) TM and (F) DM. Red outline = plasma membrane, yellow outline = nuclear membrane.

Supplementary Files

This is a list of supplementary files associated with this preprint. Click to download.

- [S1.png](#)